Bioactive Materials 31 (2024) 53–62

Contents lists available at ScienceDirect

Bioactive Materials

journal homepage: www.keaipublishing.com/en/journals/bioactive-materials

Review article

Manganese molybdate nanodots with dual amplification of STING activation for "cycle" treatment of metalloimmunotherapy

Huali Lei [a], Quguang Li [a], Guangqiang Li [a], Tianyi Wang [b], Xinjing Lv [c], Zifan Pei [a], Xiang Gao [d], Nailin Yang [a], Fei Gong [a], Yuqi Yang [a], Guanghui Hou [a], Minjiang Chen [e], Jiansong Ji [e,**], Zhuang Liu [a,***], Liang Cheng [a,*]

[a] Institute of Functional Nano & Soft Materials (FUNSOM), Jiangsu Key Laboratory for Carbon-Based Functional Materials and Devices, Soochow University, Suzhou, 215123, China
[b] Department of Neurosurgery, The First Affiliated Hospital of Soochow University, Suzhou, 215000, China
[c] Children's Hospital of Soochow University, Pediatric Research Institute of Soochow University, Suzhou, 215123, China
[d] Department of Orthopedics, The Second Affiliated Hospital of Soochow University, Suzhou, Jiangsu, 215004, China
[e] Key Laboratory of Imaging Diagnosis and Minimally Invasive Intervention Research, Fifth Affiliated Hospital of Wenzhou Medical University, Lishui, 323000, Zhejiang, China

ARTICLE INFO

Keywords:
Metalloimmunotherapy
Manganese molybdate nanoparticles
cGAS-STING pathway
DCs maturation
Ferroptosis

ABSTRACT

Certain types of cationic metal ions, such as Mn^{2+} are able to activate immune functions via the stimulator of interferon genes (STING) pathway, showing potential applications in eliciting antitumor immunity. How anionic ions interact with immune cells remains largely unknown. Herein, selecting from a range of cationic and anionic ions, we were excited to discover that MoO_4^{2-} could act as a cGAS-STING agonist and further confirmed the capability of Mn^{2+} to activate the cGAS-STING pathway. Inspired by such findings, we synthesized manganese molybdate nanoparticles with polyethylene glycol modification (MMP NDs) for cancer metalloimmunotherapy. Meanwhile, MMP NDs could consume glutathione (GSH) over-expressed in tumors and induce ferroptosis owing to high-valence Mo and Mn to elicit tumor-specific immune responses, which was further amplified by MMP-triggered the cGAS-STING activation. In turn, activated $CD8^+$ T cells to secrete high levels of interferon γ (IFN-γ) and reduced GPX4 expression in tumor cells to trigger ferroptosis-specific lipid peroxidation, which constituted a "cycle" of therapy. As a result, the metalloimmunotherapy with systemic administration of MMP NDs offered a remarkable tumor inhibition effect for a variety of tumor models. Our work for the first time discovered the ability of anionic metal ions to activate the immune system and rationally designed bimetallic oxide nanostructures as a multifunctional therapeutic nanoplatform for tumor immunotherapy.

1. Introduction

Cancer immunotherapy (CIT) can inhibit tumor growth and metastasis by activating the host's immune system to achieve anti-tumor immune responses [1–3]. Although CIT has recently achieved some clinical success, only a small percentage of patients with solid tumors would be responsive to immunotherapy [4,5]. One critical reason that leads to cancer immunotherapy failure is the immunosuppressive tumor microenvironment (TME), which features with the poor infiltration of pro-inflammatory immune cells, including tumor-infiltrating cytotoxic T lymphocytes (CTLs), pro-inflammatory M1 phenotype macrophages, and dendritic cells (DCs) [6,7]. To enhance the antitumor immune response, several cancer treatment modalities have been developed. Among them, the cGAS-STING pathway has been discovered and widely used in CIT for immune activation [8]. When cyclic GMP-AMP synthase (cGAS) detects double-stranded DNA that should not exist within the cytoplasm, it catalyzes the generation of cyclic adenylate small molecules (cGAMP) [9,10]. Meanwhile, the dimeric stimulator of interferon

Peer review under responsibility of KeAi Communications Co., Ltd.
* Corresponding author.
** Corresponding author.
*** Corresponding author.
E-mail addresses: jijiansong@zju.edu.cn (J. Ji), zliu@suda.edu.cn (Z. Liu), lcheng2@suda.edu.cn (L. Cheng).

https://doi.org/10.1016/j.bioactmat.2023.07.026
Received 24 April 2023; Received in revised form 14 July 2023; Accepted 31 July 2023

genes (STING) binds to cGAMP to change the conformation of STING, recruit and phosphorylate tank binding kinase 1 (TBK1) protein and further activate interferon regulatory factor (IRF3), which induces type I interference and activates innate immunity [11]. As malignant tumors are usually accompanied by cytoplasmic chromatin fragmentation and micronucleus formation, DNA leakage from cancer cells is significantly higher than that from normal cells, making the cGAS-STING activation particularly meaningful in cancer immunotherapy [12,13].

Recently, metal cations have attracted much attention because of their special biological effects in tumor therapy [14,15]. Importantly, manganese ions (Mn^{2+}) and zinc ions (Zn^{2+}) have the ability to activate the cGAS-STING pathway, thus them have the potential to act as immune activation agents [16,17]. Various nanoscale platforms containing Mn^{2+} or Zn^{2+} have thus been designed and constructed to further enable delivery of those metal ions together with other therapeutic molecules into tumors for CIT [16,18]. However, although the role of anionic metal ions in the cGAS-STING activation has been widely evidenced, whether metal anions have similar activities in immune activation remains largely unknown. Recently, the unique biological process induced by molybdenum proved the unique fate and important role of metal anions in living bodies [19,20]. Therefore, it would be interesting to study the immune activation possibilities of anionic ions, and based on such information, to engineer nanomedicine with immune activating metal cations and anions for anti-tumor metalloimmunotherapy.

Meanwhile, ferroptosis has been reported to be widely used to enhance CIT [21,22]. In addition to Fe-containing nanomaterials, many nanomaterials containing high-valent metals with GSH consumption function have also been used to induce ferroptosis in tumor cells, especially those containing Mo^{6+}, Mn^{7+} and V^{5+} [23–25]. Herein, we used 293-Dual™ mSTING cells to screen a variety of metal cations (Mn^{2+}, Mg^{2+}, Ca^{2+}, Zn^{2+}, Na^{+}, Cu^{2+}, and Ga^{3+}) and anions (MoO_4^{2-}, NO_3^-, WO_4^{2-}, SO_4^{2-}, Cl^-, VO_4^{3-}, and VO_3^-), and discovered that Mn^{2+} and MoO_4^{2-} had the most potent ability to activate the cGAS-STING pathway among the tested cations and anions, respectively (Scheme 1). Considering that the combination of Mn^{2+} and MoO_4^{2-} could further amplify the cGAS-STING activation, we thus designed the bimetallic oxide manganese molybdate nanoparticles (MMO NDs) constructed from Mn^{2+} and MoO_4^{2-}. With further modification by distearoyl phosphatidylethanolamine-polyethylene glycol 5000 (DSPE-PEG_{5k}), we then obtained PEGylated manganese molybdate nanoparticles (MMP NDs). Interestingly, it was found that high-valence Mo and Mn could consume GSH in the tumor and inhibit glutathione peroxidase 4 (GPX4) activity, further inducing ferroptosis [26,27]. Upon tumor cell death, MMP NDs with the cGAS-STING activation capability induced DCs maturation and further activated $CD8^+$ T cells, following with initiating anti-tumor immune responses [28,29]. In turn, activated $CD8^+$ T cells secreted interferon γ (IFN-γ) and reduced GPX4 expression in tumor cells to trigger ferroptosis mediated lipid peroxidation, which constituted a "cycle" of therapy [28,30]. As a result, MMP NDs by intravenous (i.v.) injection were able to reverse the immunosuppressive TME and simultaneously realize the dual functions of initiating CIT and enhancing CIT without the addition of any immune adjuvant. Effective tumor growth suppression with such MMP NDs was then achieved in different types of tumor models in mice, without observing significant toxic effects to mice. Our work, for the first time, used ion screening as the basis for the construction of bimetallic oxides as a cancer immunotherapy nanomedicine platform.

2. Results and discussion

2.1. Metal ions with the capability to activate the cGAS-STING pathway

293-Dual™ mSTING cells were first used to screen the abilities of metal ions to activate the cGAS-STING pathway. After transfection with the cGAS plasmids, the pretreated mSTING cells were incubated with coelenterazine-utilizing luciferase detection medium (QUANTI-Luc™). Afterwards, bioluminescence signals could be observed from the pretreated mSTING cells when they were incubated with substances with the cGAS-STING pathway activation capability [16]. Therefore, the pretreated mSTING cells were incubated with various metal cations (Mn^{2+}, Mg^{2+}, Ca^{2+}, Zn^{2+}, Na^{+}, Cu^{2+}, and Ga^{3+}), and then the bioluminescence signals from mSTING cells were detected (Fig. 1a). It was found that Mn^{2+} indeed had the strongest ability to activate the cGAS-STING pathway, followed by Zn^{2+} and Ga^{3+} (Fig. 1b). Meanwhile, a variety of anions (MoO_4^{2-}, NO_3^-, WO_4^{2-}, SO_4^{2-}, Cl^-, VO_4^{3-}, and VO_3^-) were also detected. Surprisingly, several metal anions also activated the cGAS-STING pathway (Fig. 1c), such as MoO_4^{2-} and WO_4^{2-} ions, of which MoO_4^{2-} appeared to be the most effective in the cGAS-STING activation.

To further verify the cGAS-STING pathway activation capability of Mn^{2+} and MoO_4^{2-} ions, the primary mouse bone marrow-derived

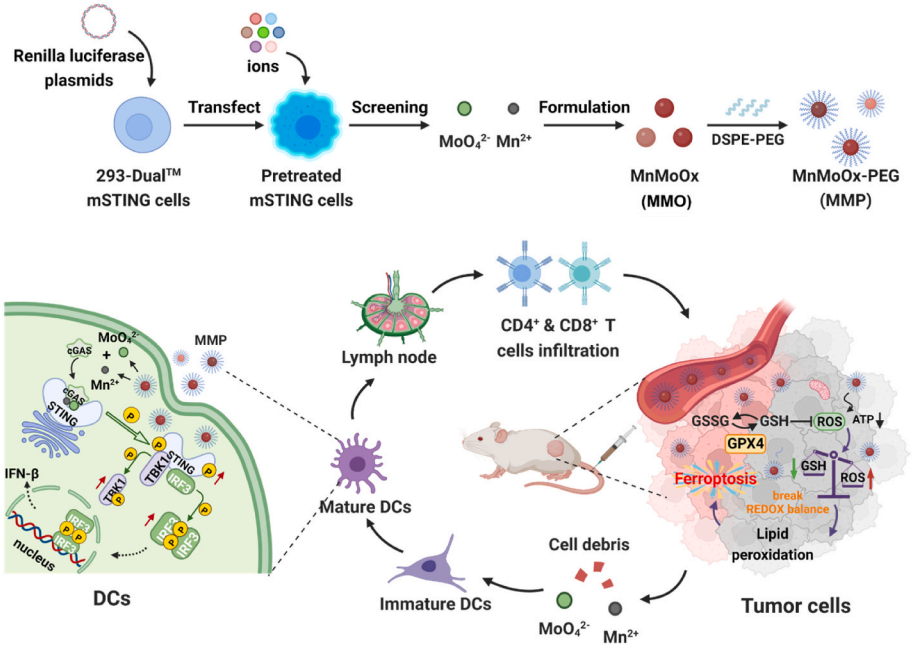

Scheme 1. MMP NDs with dual cGAS-STING activation for cancer metalloimmunotherapy. Metal cations and anions with the strongest cGAS-STING activation were screened using 293-Dual™ mSTING cells and then employed to construct bimetallic oxide MMO NDs, then MMP NDs were obtained by DSPE-PEG_{5k} modification. MMP NDs containing Mn^{2+} and MoO_4^{2-} showed effective cGAS-STING activation. After systemic administration, MMP NDs could consume the highly expressed GSH in tumor cells, break the redox balance, inhibit the activity of the GPX4 enzyme, and subsequently lead tumor cells ferroptosis. Tumor debris in the presence of MMP NDs would then trigger tumor-specific cell immunity.

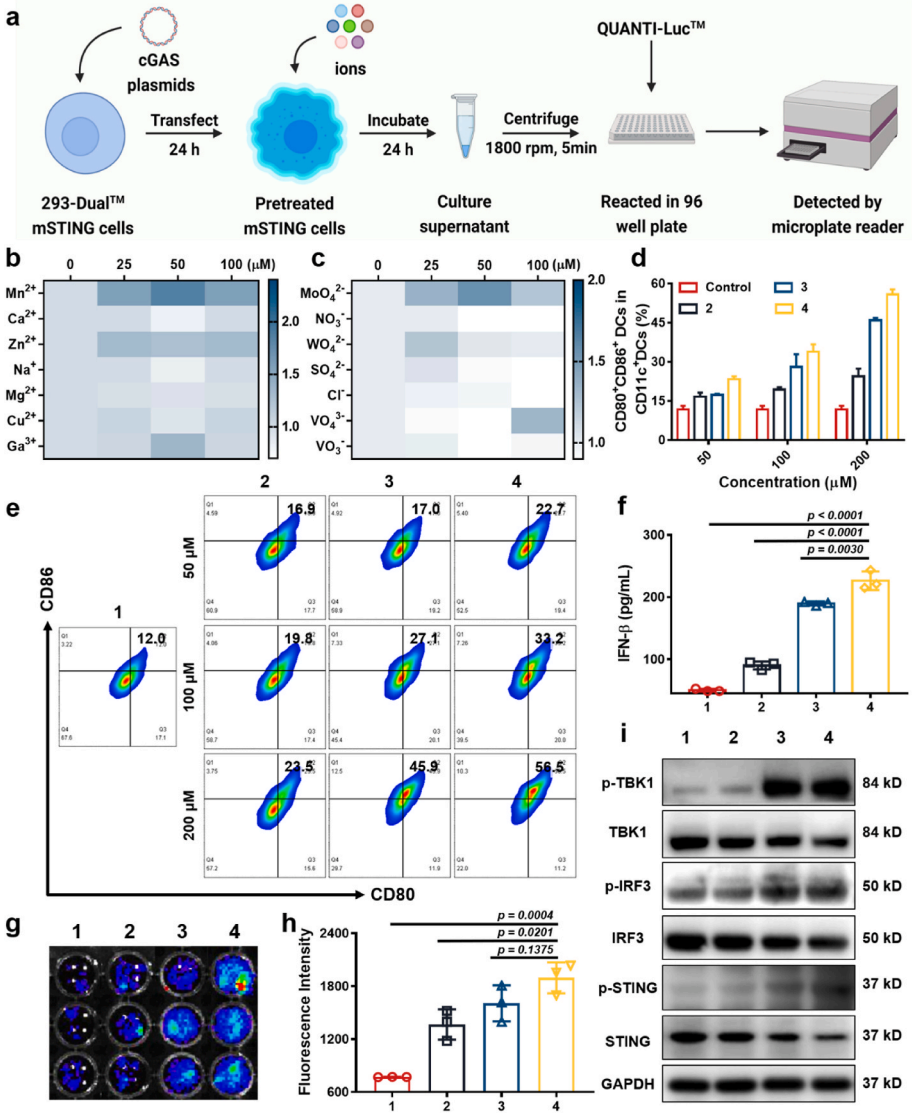

Fig. 1. Screening for ions with the ability to activate the cGAS-STING pathway. **(a)** Scheme of ion screening with 293-Dual™ mSTING cells. **(b&c)** 293-Dual™ mSTING cells containing cGAS were treated with different concentrations of metal cations (**b**) or anions (**c**). **(d)** The percentages of mature DCs in (**e**). **(e)** The detection of BMDCs maturation after incubation with different concentrations of Mn^{2+}, MoO_4^{2-} and the mixtures of Mn^{2+} and MoO_4^{2-} for 16 h. **(f)** Quantitative analysis of IFN-β secreted by DCs. **(g)** Qualification of bioluminescence intensities of mSTING cells after incubation with Mn^{2+}, MoO_4^{2-} and mixtures of Mn^{2+} and MoO_4^{2-} for 24 h. **(h)** Fluorescence intensity of mSTING cells in (**g**). **(i)** HeLa cells were incubated with Mn^{2+}, MoO_4^{2-} and mixtures of Mn^{2+} and MoO_4^{2-} for 16 h, following with WB detection of marker proteins in the cGAS-STING pathway, including TBK1/p-TBK1, STING/p-STING, and IRF-3/p-IRF-3. (1: control, 2: MoO_4^{2-}, 3: Mn^{2+}, and 4: Mn^{2+}+MoO_4^{2-}).

dendritic cells (BMDCs) were incubated with Mn^{2+} and MoO_4^{2-} ions, and the mixed solutions of Mn^{2+} and MoO_4^{2-}. Then, the proportion of matured DCs was analyzed by flow cytometry. Both MoO_4^{2-} ions and Mn^{2+} ions stimulated the maturation of DCs to a certain extent (Fig. 1d and e). Notably, the stimulation ability of the mixture of Mn^{2+} and MoO_4^{2-} ions on DCs maturation was significantly stronger than that of Mn^{2+} or MoO_4^{2-} ions alone (Fig. 1d and e), and the proportion of matured DCs was obviously increased as ion concentrations increased.

The mechanism of DCs maturation stimulated by metal ions was then carefully studied. First, the interferon-β (IFN-β) levels secreted by DCs after incubation with Mn^{2+}, MoO_4^{2-}, and a mixture of Mn^{2+} and MoO_4^{2-} ions were detected. Compared with the control group, MoO_4^{2-} ions effectively enhanced the IFN-β secretion by DCs, while the performance of Mn^{2+} ions was superior to that of MoO_4^{2-} ions, and the mixture of Mn^{2+} and MoO_4^{2-} ions showed the strongest enhancement of IFN-β secretion by DCs (Fig. 1f). Similarly, 293-Dual™ mSTING cells were also used to detect the ability of Mn^{2+}, MoO_4^{2-}, and a mixture of Mn^{2+} and MoO_4^{2-} ions to activate the cGAS-STING pathway. Compared with MoO_4^{2-} or Mn^{2+} alone, the mixture of Mn^{2+} and MoO_4^{2-} ions showed the highest capability of the cGAS-STING activation (Fig. 1g and h). At the same time, the phosphorylation levels of TBK1, STING, and IRF3 were detected by Western blot (WB) analysis in HeLa cells after incubation with Mn^{2+}, MoO_4^{2-}, or a mixture of Mn^{2+} and MoO_4^{2-} ions. The relative phosphorylation levels of the TBK1, STING, and IRF3 proteins (i.e., p-TBK1/TBK1, p-STING/STING, and p-IRF3/IRF3) in HeLa cells were remarkably increased after incubation with Mn^{2+} or MoO_4^{2-} alone, and the combination of Mn^{2+} and MoO_4^{2-} ions resulted in the highest phosphorylation levels of these three proteins, proving the effective ability of those ions to activate the cGAS-STING pathway (Fig. 1i). The above data suggested that both Mn^{2+} and MoO_4^{2-} could activate the cGAS-STING pathway by enhancing phosphorylation of STING, TBK1, and IRF3, which in turn stimulated the maturation of DCs and further secretion of IFN-β. Moreover, the combination of Mn^{2+} and MoO_4^{2-} further amplified the function of activating the cGAS-STING pathway and stimulating DCs maturation.

2.2. Synthesis of manganese molybdate nanoparticles and their cGAS-STING activation capacity

Inspired by the above findings, we then designed manganese molybdate nanoparticles constructed by both Mn^{2+} and MoO_4^{2-} for the cGAS-STING pathway activation. A simple high-temperature solution method was employed to synthesize manganese molybdate nanodots (MnMoOx, MMO NDs), that contain different valences of Mo and Mn (Supplementary Fig. S1). Transmission electron microscopy (TEM) showed ultrasmall nanodots with a size of ~5 nm (Fig. 2a). The main

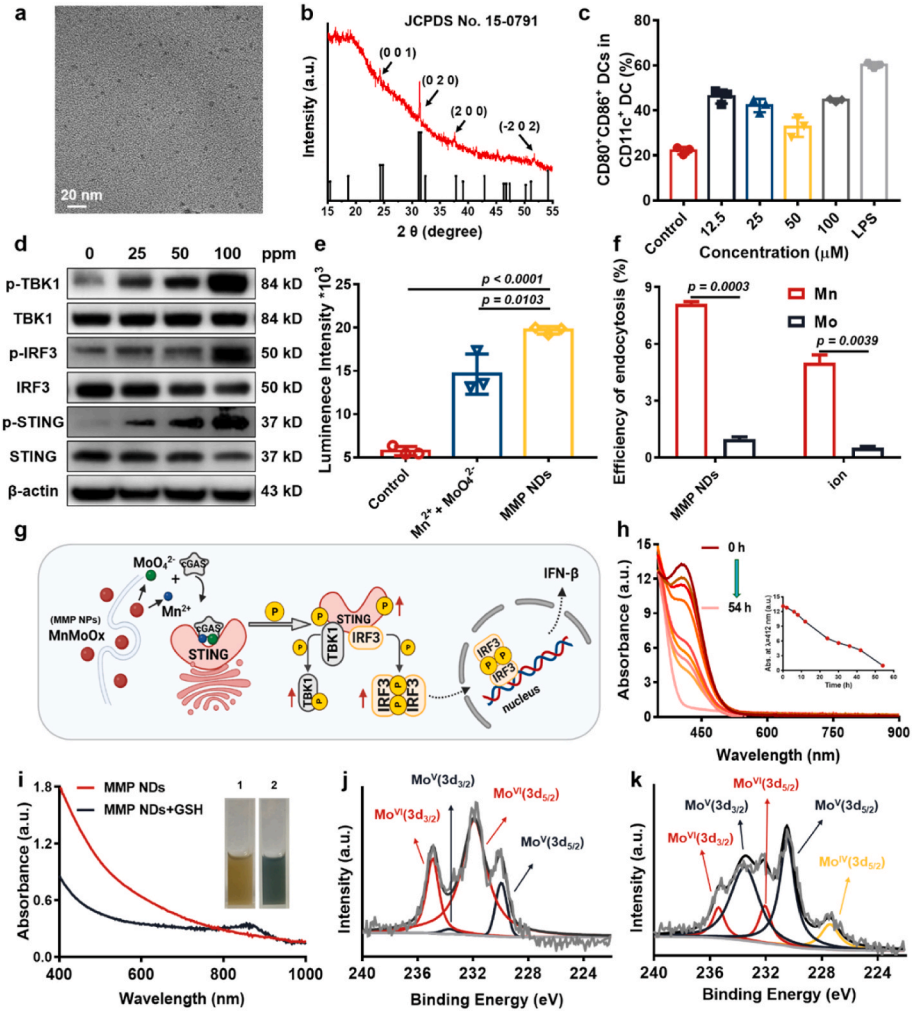

Fig. 2. Characterization and properties of MMP NDs. (a) TEM image of MMO NDs. **(b)** XRD patterns of MMO NDs. **(c)** The detection of BMDCs maturation ($CD80^+CD86^+$ cells among $CD11c^+$ DCs) after incubation with MMP NDs for 16 h. **(d)** HeLa cells were incubated with different concentrations of MMP NDs for 16 h, followed by WB for marker proteins in the STING–IFN–β pathway including TBK1/p-TBK1, STING/p-STING, and IRF-3/p-IRF-3. **(e)** Quantification of the bioluminescence intensities of mSTING cells after incubation with MMP NDs and the mixtures of Mn^{2+} and MoO_4^{2-} for 24 h. **(f)** The cellular uptake of Mn^{2+} or MMP NDs by HeLa cells was detected by ICP-MS. **(g)** Illustration showing that MMP NDs after endocytosis may be gradually decomposed into Mn^{2+} and MoO_4^{2-}, which would activate the cGAS-STING pathway. NDs. **(h)** Time-dependent GSH (1 mM) consumption by MMP NDs. **(i)** UV absorption and optical photos of MMP NDs before and after reaction with GSH, 1) MMP NDs, 2) MMP NDs + GSH. **(j&k)** XPS of Mo in MMP NDs before (**j**) and after (**k**) reaction with GSH.

characteristic peaks of MMO NDs obtained by X-ray powder diffraction (XRD) were consistent with the cubic structure of $MnMoO_4$ (JCPDs. 15–0791) (Fig. 2b). After that, MMO NDs were modified with the amphiphilic polymer $DSPE\text{-}PEG_{5k}$ to obtain PEGylated manganese molybdate NDs (MMP NDs) (Supplementary Fig. S1), and the hydrodynamic particle size of MMP NDs was measured to be ~10 nm (Supplementary Fig. S2). After being dispersed in H_2O, 0.7% NaCl, PBS, and 1640 cell culture medium for 7 days, no obvious precipitation was found, indicating the good stability of those nanoparticles in these physiological solutions (Supplementary Fig. S3). Meanwhile, the Mn^{2+} release from MMP NDs was detect to further verification of its stability. It was found that only ~28% of Mn^{2+} released over 72 h, indicating the good stability of MMP NDs in water (Supplementary Fig. S4).

Next, the stimulating ability of MMP NDs on DCs maturation was tested. The proportion of mature DCs was detected after incubation with different concentrations of MMP NDs. An obvious increase in mature DCs was observed after their incubation with MMP NDs, proving that the ability of MMP NDs to stimulate DCs maturation (Fig. 2c and Supplementary Fig. S5). Furthermore, proinflammatory cytokines such as tumor necrosis factor-α (TNF-α), interleukin-6 (IL-6), and interleukin-12p70 (IL-12p70) secreted by DCs after incubation with MMP NDs was detected. Incubation with MMP NDs promoted the secretion of TNF-α, IL-6, and IL-12p70 proinflammatory cytokines by DCs, which further activated systemic antitumor immune responses (Supplementary Fig. S6). Similarly, WB analysis was also used to explore the activation of the cGAS-STING pathway by MMP NDs. With the increased concentrations of MMP NDs, the relative phosphorylation levels of TBK1, STING, and IRP3 in treated cells were remarkably enhanced (Fig. 2d). Meanwhile, 293-Dual™ mSTING cells were used to evaluate the ability of MMP NDs to activate the cGAS-STING pathway. It could be found that compared to the mixture of Mn^{2+} and MoO_4^{2-} ions at the same concentration, MMP NDs showed a stronger ability to activate the cGAS-STING pathway (Fig. 2e). Notably, compared to the mixture of Mn^{2+} and MoO_4^{2-} ions, MMP NDs with the same Mn and Mo contents showed greatly enhanced cellular uptake, likely via nanoparticle endocytosis (Fig. 2f). Moreover, the decomposition ability of MMP NDs in aqueous solution and GSH solution were also investigated. It was found that in aqueous solution ~28% Mn^{2+} released from MMP NDs for 72 h, while ~75% Mn^{2+} released from MMP NDs in the solution containing GSH (Supplementary Fig. S4). Therefore, we hypothesized that MMP NDs with increased cellular uptake could be decomposed into Mn^{2+} and MoO_4^{2-} (Fig. 2g), which would further promote the phosphorylation of TBK1, STING, and IRP3, and subsequently enable the cGAS-STING activation.

2.3. MMP NDs with GSH consumption capacity to induce ferroptosis

GSH, as a highly expressed substance in the TME, can resist the invasion of external reactive oxygen species (ROS), thus affecting the antitumor effect of exogenous ROS [31]. Recently, it was found that consuming intracellular GSH could break the intracellular redox balance, down-regulate GPX4 expression, lead to cell lipid peroxidation, and thus induce cell ferroptosis [32]. Due to the existence of high valence Mo^{6+} and Mn^{4+}, which could be reduced by GSH to form a low

valence state of Mo^{5+} and Mn^{2+}, we speculated that MMP NDs might have a good GSH consumption capacity to realize ferroptosis. Therefore, the GSH consumption ability of MMP NDs was evaluated by a 5, 5′-dithiobis-(2-nitrobenzoic acid) (DTNB) probe [33]. With the extension of the incubation time, the UV–Vis characteristic absorption peak of DTNB at ~ 412 nm showed a significant decrease, demonstrating the effective GSH consumption ability of MMP NDs (Fig. 2h). At the same time, MMP NDs changed from brown-yellow to blue in color, and showed an obvious absorption peak at ~808 nm after incubation with GSH, probably due to the change of Mo valence state (Fig. 2i). Therefore, X-ray photoelectron spectroscopy (XPS) was used to detect the valence state of Mo in MMP NDs before and after GSH reduction. The $Mo^{V}(3d_{3/2})$ at ~ 233.7 eV and $Mo^{V}(3d_{5/2})$ at ~ 229.95 eV increased to ~ 38.62% and ~34.45% after incubation with GSH, respectively, whereas Mo^{VI} $(3d_{3/2})$ at ~ 234.91 eV and Mo^{VI} $(3d_{5/2})$ at ~ 231.90 eV decreased to ~ 7.75% and ~9.52%, respectively (Fig. 2j and k). Meanwhile, the XPS of Mn in MMP NDs before and after GSH reaction were assayed to confirm the role of Mn in GSH consumption. The percentage of high valence state $Mn^{IV}(2p_{3/2})$ was deceased from ~20.80% to ~ 11.50% and $Mn^{III}(2p_{3/2})$ was deceased from ~48.2% to ~ 46.22%, while the percentage of low valence state $Mn^{II}(2p_{1/2})$ was increased from ~30.07% to ~ 40.03%, and $Mn^{0}(2p3_{/2})$ was increased from 1.11% to 2.25% (Supplementary Fig. S7). All these results demonstrated that Mo and Mn with the high valence states in MMP NDs could act as an oxidative agent to consume GSH, which provides the potential to induce iron death in tumor cells.

Next, we studied how MMP NDs interact with cells *in vitro*. First, the endocytosis of MMP NDs by cells was carefully examined. Mouse colon cancer cells (CT26) were incubated with Cy5.5 labeled MMP NDs (MMP-Cy5.5 NDs) for various periods of time. The red intracellular signals were significantly increased with the extension of incubation time, indicating that MMP NDs could be endocytosed into cells (Fig. 3a and Supplementary Fig. S8). At the same time, the apoptosis level of CT26 cells treated with MMP NDs was detected by the apoptosis kit. After incubation with MMP NDs, the levels of early apoptosis increased from ~2.43% to ~24.60%, while the late apoptosis changed from ~2.34% to ~20.20% (Fig. 3d and e and Supplementary Fig. S9). Next, the killing effect of MMP NDs on normal cells, such as human umbilical vein endothelial cells (HUVECs) and mouse dendritic cells 2.4 (DC2.4), as well as tumor cells, including CT26 cells, mouse melanoma cells (B16F10), and mouse breast cancer cells (4T1), were carefully investigated. The cells were incubated with different concentrations of MMP NDs before the cell viability assay. Compared with the normal cells (HUVECs and DC2.4), the MMP NDs showed a stronger killing effect on the tested tumor cells (Fig. 3b and c). The half-maximal inhibitory concentrations (IC_{50}) of MMP NDs for CT26 cells, 4T1 cells, and B16F10 cells were ~26.16 ± 5.33, ~52.98 ± 6.93, and ~104.93 ± 4.80 ppm, respectively (Supplementary Fig. S10), probably due to the diverse contents of GSH in these cancer cells. To confirm this, the GSH content in these tumor cells were detected by DTNB probe. The GSH content was highest in CT26 cells, followed by 4T1 cells, and the lowest in B16F10 cells (Supplementary Fig. S11), further confirming the different killing effects of MMP NDs.

Next, the ferroptosis induced by MMP NDs in tumor cells was investigated. CT26 cells were treated with MMP NDs for various time and then stained with 2,7-dichlorodihydrofluorescein diacetate (DCFH-DA) and ThiolTracker Violet probes to detect intracellular ROS and GSH, respectively. With prolonged incubation time, the ROS signals into cytoplasm were dramatically increased, while the GSH signals into nucleus showed a remarkable decrease (Fig. 3g and Supplementary Fig. S12). These results indicated that MMP NDs could consume intracellular GSH, break their redox balance, and increase intracellular ROS levels.

Afterwards, the lipid hydroperoxide (LPO) probe was used to determine the lipid peroxidation levels of tumor cells after treatment with MMP NDs. CT26 cells were incubated with MMP NDs and then stained with an LPO probe. An extraordinary enhancement of green signals in CT26 cells was observed, as the MMP NDs concentrations increased, proving that MMP NDs could promote lipid peroxidation of cells (Supplementary Fig. S13). Then, malondialdehyde (MDA) level were further determined with a MDA kit, which is the end product of the lipid oxidation. MMP NDs treated CT26 cells were broken by ultrasound irradiation before MDA was extracted. With increasing MMP NDs concentrations, the UV characteristic absorption peak of malondialdehyde-thiobarbituric acid (MDA-TBA) at ~ 535 nm showed an obvious increase

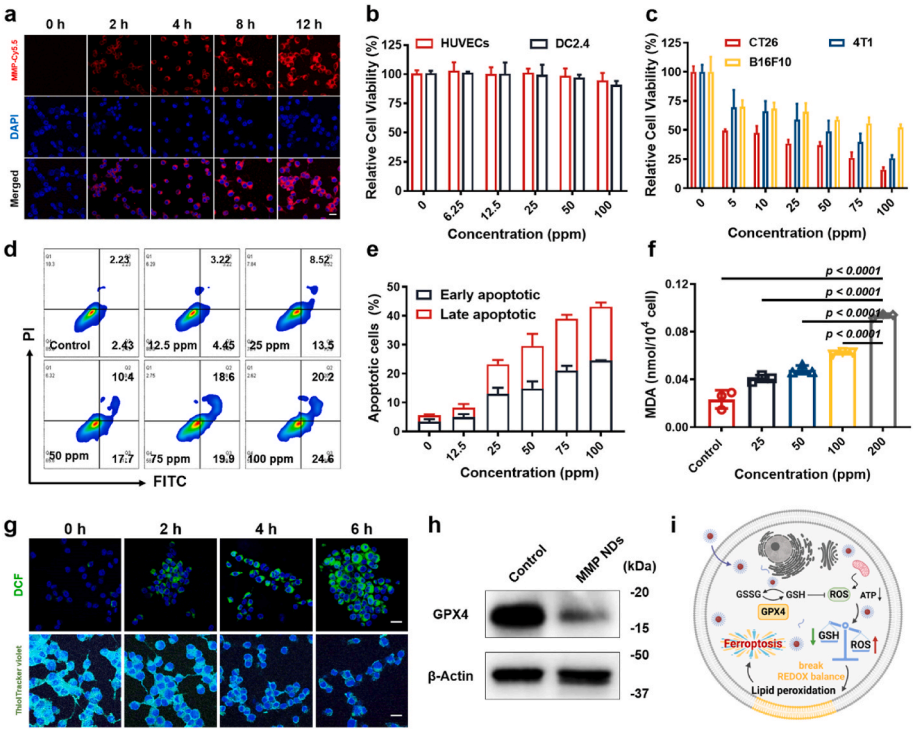

Fig. 3. MMP NDs induced ferroptosis. (a) Endocytosis of MMP-Cy5.5 NDs (scale bar: 20 μm). **(b&c)** Relative viabilities of (**b**) normal cells (HUVECs and DC2.4) and (**c**) tumor cells (CT26, 4T1 and B16F10) after incubation with different concentrations of MMP NDs for 12 h. **(d)** Apoptosis detection of CT26 cells after incubation with MMP NDs. **(e)** Statistical data of apoptosis in (**d**). **(f)** MDA content in MMP NDs treated CT26 cells. **(g)** MMP NDs treated CT26 cells were stained with DCFH-DA and ThiolTracker violet probe (scale bar: 20 μm). **(h)** The expression of GPX4 in MMP NDs treated CT26 cells was evaluated by WB. **(i)** Scheme of ferroptosis of tumor cells triggered by MMP NDs.

(Fig. 3f, Supplementary Fig. S14), indicating lipid peroxidation triggered by MMP NDs in CT26 cells.

Next, a WB assay was used to detect GPX4 expression in MMP NDs-treated tumor cells. After CT26 cells were treated with MMP NDs, the expression level of GPX4 in CT26 cells was markedly decreased, proving that MMP NDs could effectively reduce the level of GSH in tumor cells and inactivate GPX4 (Fig. 3h). The change in mitochondrial membrane potential is an important indicator of ferroptosis [34–36]. When ferroptosis occurs in cells, the membrane potential is significantly reduced or even lost. Therefore, the 5,5,6,6-tetrachloro-1,1,3,3-tetraethylimidacarbocyanine iodide (JC-1) probe was used to detect changes in the mitochondrial membrane potentials of tumor cells before and after MMP NDs treatment. The aggregated JC-1 probes (red fluorescence) and JC-1 monomers (green fluorescence) stained on the mitochondrial membrane could indicate the normal mitochondrial membrane potential as well as the disturbed one, respectively [37]. Thus, CT26 cells were incubated with MMP NDs, followed by JC-1 staining. It could be found that the higher concentrations of MMP NDs induced more obvious red fluorescence signals, evidencing considerable disturbance in the mitochondrial membrane potentials of MMP NDs treated CT26 cells (Supplementary Fig. S15). Above all, after entering tumor cells, MMP NDs decomposed into Mn^{2+} and MoO_4^{2-}, enabling intracellular GSH consumption, breaking their redox balance, and increasing the intracellular ROS level. Then, the mitochondrial respiration was inhibited and GPX4 enzyme was inactivated, which led to lipid peroxidation of tumor cells and finally triggered cell ferroptosis (Fig. 3i). In conclusion, MMP NDs not only induced ferroptosis by depleting GSH in tumor cells, but also stimulated DCs maturation by activating the cGAS-STING pathway and further activated $CD8^+$ T cells. IFN-γ released from $CD8^+$ T cells further induced ferroptosis in tumor cells, and the ferroptosis tumor cells further stimulated DCs maturation by releasing DAMPs.

2.4. Systemic administration of MMP NDs in CT26 tumor models

Inspired by the good performance of MMP NDs *in vitro*, the capability of MMP NDs to suppress tumors and activate the cGAS pathway *in vivo* was next investigated. First, the biodistribution of MMP NDs was studied after i.v. injection. After being injected for 24 h, ~10.5% ID/g MMP NDs was enriched in the tumor site, which proved their good tumor enrichment effect (Supplementary Fig. S16). Moreover, the blood circulation study further verified the good circulation ability of MMP NDs after i.v. injection. Moreover, the blood circulation study further verified the good circulation ability of MMP NDs after i.v. injection. The half-life time of $t_{1/2\alpha}$ and $t_{1/2\beta}$ was calculated to be 1.298 ± 0.082 h and 5.019 ± 0.234 h, respectively, indicating a good blood circulation of MMP NDs (Supplementary Fig. S17). Next, the CT26 tumor bearing BALB/c mice were randomly divided into 4 groups when the mean tumor volume reached ~100 mm^3: 1) control, 2) intravenous (i.v.) injection of MMP

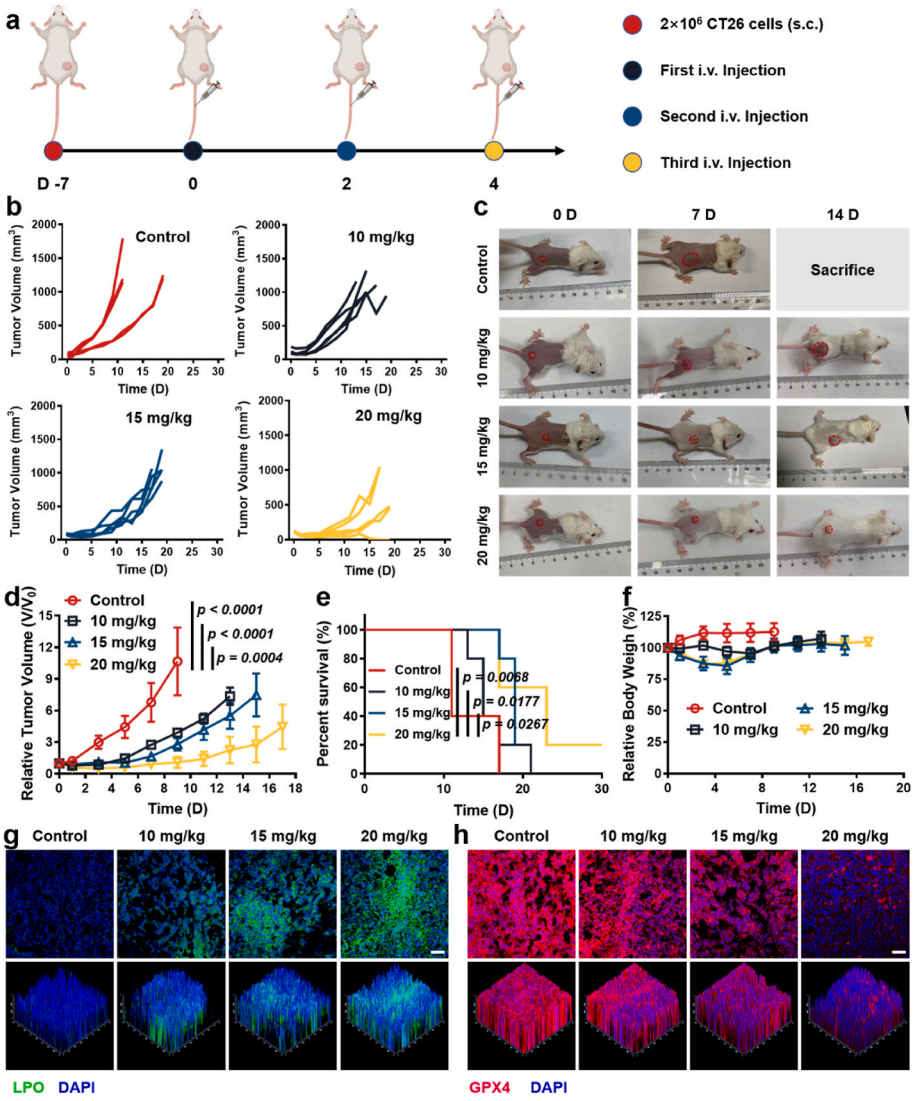

Fig. 4. Systemic administration of MMP NDs to treat CT26 tumors. (a) Scheme of systemic administration of MMP NDs in CT26 tumor bearing mice. **(b)** Tumor sizes of mice after various treatments, including 1) control, 2) MMP NDs (i.v. 10 mg/kg), 3) MMP NDs (i.v. 15 mg/kg) and 4) MMP NDs (i.v. 20 mg/kg). **(c)** Optical photos of mice after various treatments in (**b**). **(d)** Relative CT26 tumor volume in (**b**). **(e)** Percent survival of mice in (**b**). **(f)** Relative body weights of the mice with different treatments in (**b**). **(g&h)** Fluorescence images of tumor slices after staining with LPO (**g**) and GPX4 (**h**) (scale bar: 50 μm).

NDs (10 mg/kg), 3) i.v. injection of MMP NDs (15 mg/kg), and 4) i.v. injection of MMP NDs (20 mg/kg). MMP NDs were i.v. injected on days 0, 2, and 4 (Fig. 4a). Compared with the control group, three doses of MMP NDs injections showed an excellent tumor growth inhibition effect, and MMP NDs exhibited increased antitumor effects with the enhancement of the injection dose (Fig. 4b–d). The survival of mice was significantly prolonged with multiple injections of MMP NDs (Fig. 4e). It was found that MMP NDs with i.v. injection could lead to body weight loss, especially after the second and third injections (Fig. 4f). However, the body weights of the mice recovered when the injection of MMP NDs stopped. Meanwhile, hematoxylin and eosin (H&E) staining of tumor sections was further used to verify the tumor killing effect of MMP NDs. The nuclei of the tumor cells appeared significantly wrinkled and the number of nuclei was also reduced after MMP NDs treatment, and it also showed better excellent effects with increasing doses of MMP NDs, further indicating that MMP NDs effectively killed cells (Supplementary Fig. S18). Furthermore, we verified the ability of MMP NDs by i.v. injection to induce tumor ferroptosis. LPO and GPX4 probes were used to characterize the lipid peroxidation level and GPX4 expression level of the tumor. The LPO signals in tumor sections were notably enhanced with increasing doses of MMP NDs, indicating that the systemic tumor treatment with MMP NDs could significantly improve the level of lipid peroxidation (Fig. 4g). In contrast, a remarkable weakening signal with red fluorescence in the tumor sections was observed with increasing injection doses of MMP NDs, proving that the GPX4 activity in the tumor site gradually decreased (Fig. 4h). In conclusion, systemic tumor treatment with MMP NDs effectively triggered lipid peroxidation and ferroptosis in tumors, which played an important role in inhibiting tumor growth and prolonging survival.

Next, to determine the mechanism of the antitumor effects induced by systemic metalloimmunotherapy, the responses of the tumor immune microenvironment induced by systemic administration of MMP NDs were evaluated. After three i.v. injections of MMP NDs, the mice were sacrificed on the 7th day, and the tumors and tumor-draining lymph nodes (TDLNs) were harvested to make single-cell suspensions for detection (Fig. 5i). The proportion of mature DCs in the lymph nodes effectively promoted from ~15.4% to ~19.8% (10 mg/kg), ~23.2% (15 mg/kg), and ~30.2% (20 mg/kg), respectively (Fig. 5a). At the same time, the proportion of $CD11b^{+}MHC\ II^{+}$ DCs in $CD11c^{+}$ (mature DCs) DCs in tumors was extraordinarily higher than that in the control group, and an effective enhancement of the mature DCs level was observed with the dose increase, proving that MMP NDs could activate the cGAS-STING pathway and stimulate the maturation of DCs both in TDLNs and tumor sites after systemic administration, on account of Mn^{2+} and MoO_4^{2-} in MMP NDs (Fig. 5b). Moreover, infiltration of M1-type macrophages with antitumor function in tumors showed a significant increase with the injection dose (Fig. 5c). The infiltration of M2-type macrophages with tumor growth promoting function was remarkably decreased, demonstrating that systemic injection of MMP NDs could regulate the polarization of the macrophage phenotype from M2-type to M1-type, providing support for the subsequent systemic activation of anti-tumor immune microenvironment (Fig. 5d). At the same time, the $CD3^{+}$ T

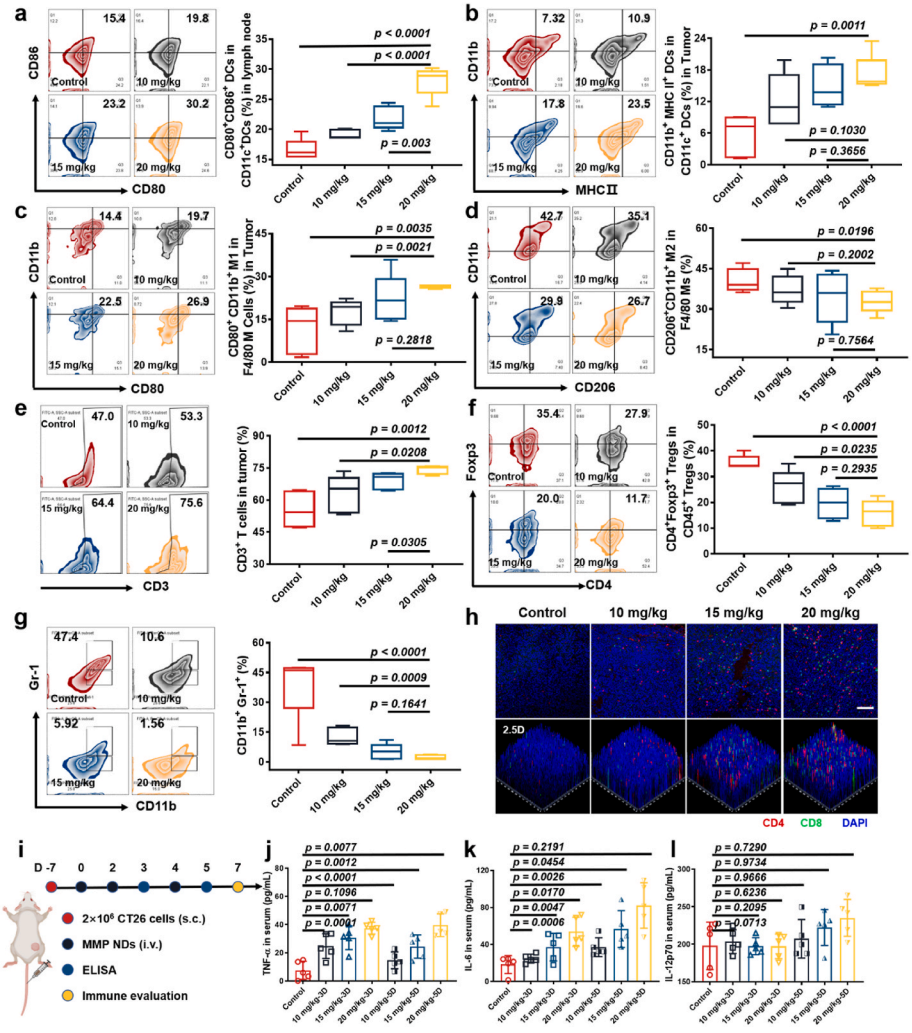

Fig. 5. ***Evaluations of the immune responses triggered by MMP NDs in mice.*** **(a–g)** Flow cytometric plots for the analysis of DC maturation in the TDLNs (**a**), DC maturation in tumors (**b**), $CD11b^{+}$ $CD80^{+}$ M1 macrophages in tumors (**c**), M2 cells in tumors (**d**), $CD3^{+}$ T cells (**e**), Tregs in tumors (**f**) and $CD11b^{+}Gr\text{-}1^{+}$ MDSCs in tumors (**g**). **(h)** Immunofluorescence staining images showing $CD4^{+}CD8^{+}$ T cells in CT26 tumors (scale bar: 100 μm). **(i)** Scheme of immune evaluation after various treatments in CT26 tumor bearing mice. **(j–l)** TNF-α (**j**), IL-6 (**k**) and IL-12p70 (**l**) level in sera from mice post MMP NDs treatment on the day 3 and 5.

cell infiltration was also significantly increased at the tumor site, and the $CD8^+$ T cells percentage in $CD3^+$ T cells was effectively enhanced (Fig. 5e and h and Supplementary Fig. S19). In contrast, the infiltration of Tregs, which has an immunosuppressive function, was markedly down-regulated, favorable for anti-tumor immune responses (Fig. 5f). Myeloid-derived suppressor cells (MDSCs) can promote tumor development by promoting tumor-related immunosuppression in the TME. More importantly, MDSCs ($CD11b^+Gr\text{-}1^+$) infiltration at the tumor site was significantly reduced with the increasing dose, while the infiltration of granulocyte/tumor-associated neutrophils ($CD11b^+Gr\text{-}1^{hi}Ly6C^{int}Ly6G^+$), mononuclear myeloid suppressor cells (M-MDSCs, $CD11b^+Gr\text{-}1^{int}$ $Ly6C^{hi}Ly6G^-$) and granuloid myeloid suppressor cells (G-MDSC, $CD11b^+Gr\text{-}1^{int}Ly6C^{int}Ly6G^+$) was also markedly down-regulated (Fig. 5g, Supplementary Figs. S20 and S21). All of the above results indicated that systemic administration of MMP NDs could effectively reverse the immunosuppressive tumor microenvironment.

Next, the pro-inflammatory cytokines level in the blood of MMP NDs i.v. injected mice were detected to evaluate systemic immune activation by i.v. injected MMPs. Blood samples were collected 12 h after the second and the third i.v. injection of MMP NDs on the 3rd day and 5th day, and the levels of the pro-inflammatory cytokines, including TNF-α, IL-6, and IL-12p70, were detected in the serum samples. Significant increases in TNF-α and IL-6 were observed on different days post i.v. injection of MMP NDs, while IL-12p70 levels were effectively enhanced after the third injection (Fig. 5j–l). The above results confirmed that the intravenous metalloimmunotherapy of MMP NDs could activate the systemic immune response of mice and reverse the immunosuppressive microenvironment. Notably, the elevated cytokine levels remained on the same order of magnitude compared to the control group, indicating that MMP-based metalloimmunotherapy would have a low risk of triggering cytokine storms, in which the pro-inflammatory cytokine levels would be several orders of magnitude above the normal ranges [38,39].

Moreover, to study the *in vivo* toxicity of MMP NDs, blood samples of mice were taken on the 1st day and 14th day after i.v. injection of MMP NDs, and the blood biochemical and routine tests were carried out. There was no significant difference between the control group and mice after i.v. injection of MMP NDs examined on the 1st day and 14th day, indicating that i.v. injection of MMP NDs would be relatively safe (Supplementary Fig. S22). Moreover, mice were sacrificed on the 7th day, and the main organs (heart, liver, spleen, lung, and kidney) were harvested and stained with H&E. There was no obvious organ damage after various treatments, even when the dose reached 20 mg/kg (Supplementary Fig. S23), suggesting that i.v. injected MMP NDs at the current doses would be tolerable to mice. Overall, systemic immunotherapy with MMP NDs containing Mn^{2+} and MoO_4^{2-} could induce ferroptosis of tumor cells, stimulate DCs maturation in both tumors and TDLNs, and increase $CD8^+$ T cell infiltration, which greatly promoted the anti-tumor immune responses. In turn, activated $CD8^+$ T cells secreted IFN-γ and reduced GPX4 expression in tumor cells to trigger ferroptosis, which constituted a "cycle" of therapy.

2.5. Systemic administration of MMP NDs to treat 4T1 and B16F10 tumors in mice

To verify the universality of MMP NDs for systemic immunotherapy, we selected two other tumor models, the 4T1 tumor model and B16F10 tumor model, for metalloimmunotherapy. The mice were treated when the average tumor volume of 4T1 tumor-bearing mice reached ~100 mm^3, or the average tumor volume of B16F10 tumor-bearing mice reached 50 mm^3 (Figs. 6a and 7a), and the tumor volume and body weight of mice were recorded every two days.

In the 4T1 tumor model, i.v. injection of MMP NDs effectively inhibited tumor growth, and the treatment effect became more obvious with increasing NDs doses (Fig. 6b and e, Supplementary Figs. S24 and S25). Meanwhile, MMP NDs were also effective in prolonging survival in 4T1 tumor bearing mice (Fig. 6c). Furthermore, Ki67 staining, a proliferating cell-associated antigen, and H&E staining were also used to characterize the therapeutic effect of MMP NDs. The nuclei of tumor

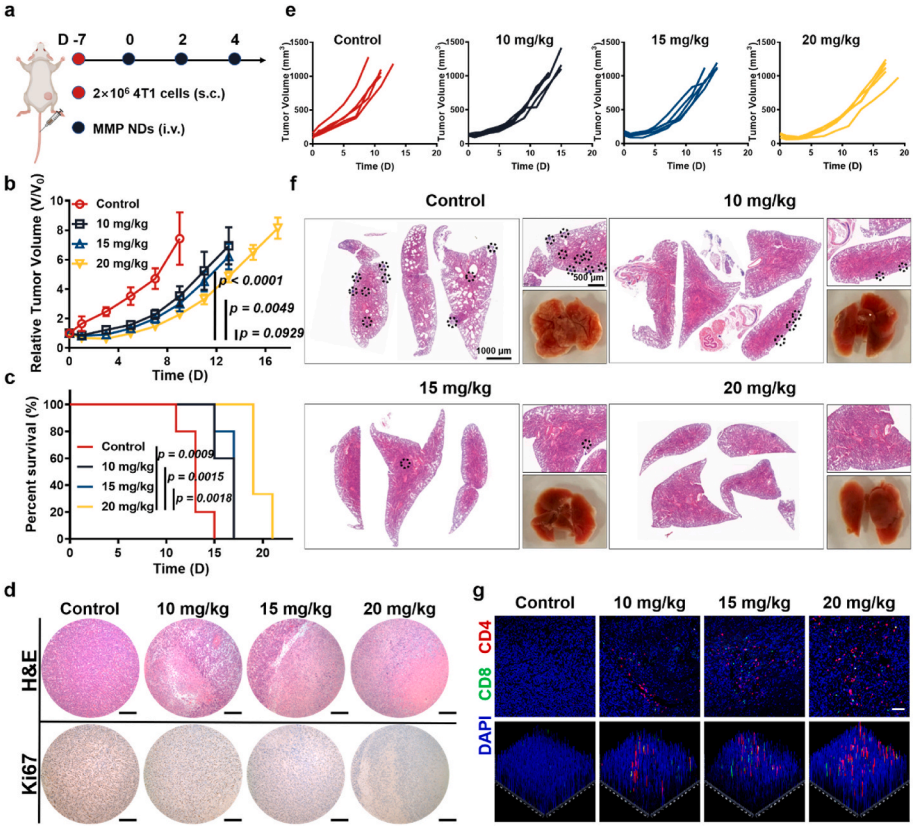

Fig. 6. Systemic administration of MMP NDs to treat 4T1 tumors. (a) Scheme of systemic administration of MMP NDs in 4T1 tumor bearing mice. **(b)** Relative 4T1 tumor volume in (**e**). **(c)** Percent survival of mice in (e). (**d**) Images of 4T1 tumor slices after staining with H&E and Ki67 (scale bar: 200 μm). **(e)** Tumor sizes of mice with 4T1 tumors after various treatments, including 1) control, 2) MMP NDs (i.v. 10 mg/kg), 3) MMP NDs (i.v. 15 mg/kg) and 4) MMP NDs (i.v. 20 mg/kg). **(f)** H&E staining images of lungs collected from mice after various treatments in (**e**). **(g)** $CD4^+CD8^+$ T cells in $CD3^+$ T cells in 4T1 tumors.

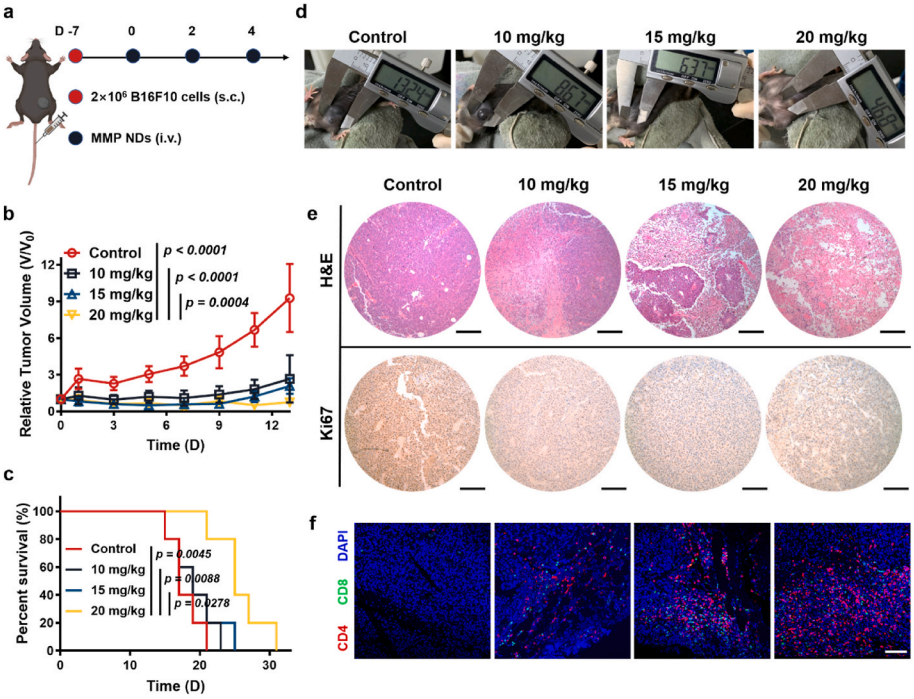

Fig. 7. Systemic administration of MMP NDs to treat B16F10 tumors. **(a)** Scheme of systemic administration of MMP NDs in B16F10 tumor bearing mice. **(b)** Relative B16F10 tumor volume in **(d)**. **(c)** Percent survival of mice in **(d)**. **(d)** Optical photos of mice bearing B16F10 tumors after various treatments including 1) control, 2) MMP NDs (i.v. 10 mg/kg), 3) MMP NDs (i.v. 15 mg/kg) and 4) MMP NDs (i.v. 20 mg/kg). **(e)** Images of B16F10 tumor slices after staining with H&E and Ki67 (scale bar: 200 μm). **(f)** $CD4^+CD8^+$ T cells in $CD3^+$ T cells in B16F10 tumors (scale bar: 100 μm).

cells shrank more obviously with increasing MMP NDs dose, indicating that tumor cells were significantly damaged in the 4T1 model after the systemic administration of MMP NDs (Fig. 6d). In contrast, a remarkable reduction in the brown Ki67 signal was observed in the MMP NDs treatment group, showing that MMP NDs could effectively inhibit the proliferation of 4T1 cells (Fig. 6d). Furthermore, the tumor sections of mice were stained with CD4 (red signal) and CD8 (green signal), and it was found that the infiltration of $CD4^+$ T cells and $CD8^+$ T cells in tumor sections also significantly increased the MMP NDs dose (Fig. 6g). All these results indicated that the systemic administration of MMP NDs had activated a good anti-tumor immune response in the 4T1 model.

Notably, the 4T1 model was a very metastatic model, and the lung samples from mice on the 7^{th} day were collected. The number of metastases was significantly inhibited in the MMP NDs treatment group. More surprisingly, there were no obvious metastases in the lung tissues of mice treated with 20 mg/kg MMP NDs (Fig. 6f). At the same time, the similar results could also be seen from H&E staining of the lung, indicating that the systemic administration of MMP NDs could not only inhibit the growth of primary tumors, but also restrain the formation of the metastatic tumors by metalloimmunotherapy triggered by MMP NDs (Fig. 6f). For the B16F10 model, systemic administration of MMP NDs also effectively inhibited tumor growth and prolonged the survival time of mice (Fig. 7b–d, Supplementary Fig. S26). As shown by H&E stained tumor sections, tumor nucleus shrinkage was more obvious with increasing MMP NDs dose, indicating more serious tumor cell damage triggered by MMP NDs treatment (Fig. 7e). As shown by Ki67 stained tumor sections, a significant weakening of the brown signals in tumor sections was observed with increasing MMP NDs doses, verifying that the proliferation ability of tumor cells was prominently inhibited by MMP NDs (Fig. 7e). At the same time, the tumor infiltration of $CD4^+$ and $CD8^+$ T cells in the MMP NDs treatment group was markedly increased, and the enhancement was more obvious with the higher dose (Fig. 7f, Supplementary Fig. S27). In general, the systemic administration of MMP NDs for metalloimmunotherapy also demonstrated significant antitumor effects to treat both 4T1 and B16F10 tumor models, promoting antitumor immune responses and inhibiting the occurrence of metastases.

3. Conclusion

In summary, a unique type of bimetallic oxide manganese molybdate nanoparticles (MMP NDs) based on two metal ions, Mn^{2+} and MoO_4^{2-}, both with the cGAS-STING activation functions, were constructed for the "cycle" treatment of tumor ferroptosis and cancer metalloimmunotherapy. Compared with bare Mn^{2+} or MoO_4^{2-}, the obtained MMP NDs composed of those two types of ions showed further enhanced the cGAS-STING activation ability. Meanwhile, those MMP NDs with GSH consumption function due to the high valence state of Mo and Mn could break the redox equilibrium and trigger ferroptosis in tumor cells. Therefore, MMP NDs post systemic intravenous injections could induce ferroptosis of tumor cells to initiate cancer metalloimmunotherapy and amplify anti-tumor immune responses via the cGAS-STING activation to further enhance cancer metalloimmunotherapy, without obvious *in vivo* toxicity. As a result, effective tumor growth suppression was realized by those MMP NDs, as demonstrated in different types of tumor models. Our work, for the first time, uses ion screening as the basis for the rational design and construction of bimetallic oxide nanomedicine for metalloimmunotherapy, offering new possibilities for the use of bioactive inorganic nanomaterials in the treatment of cancer and possibly other immune-related diseases.

Ethics approval and consent to participate

Ethics Committee (Soochow University Laboratory Animal Center) has approved the animal experiments.

Declaration of competing interest

The authors declare that they have no known competing financial interests or personal relationships that could have appeared to influence the work reported in this paper.

Acknowledgements

This article was partially supported by the National Research Programs of China (2022YFB3804604, 2021YFF0701800), National

Natural Science Foundation of China (U20A20254, 52072253), Collaborative Innovation Center of Suzhou Nano Science and Technology, the 111 Project, Joint International Research Laboratory of Carbon-Based Functional Materials and Devices, a Jiangsu Natural Science Fund for Distinguished Young Scholars (BK20211544) and Jiangsu Social Development Project (BE2019658), and Suzhou Key Laboratory of Nanotechnology and Biomedicine. The authors also thank the website app.Biorender.com for the assistance in creating the Figures.

Appendix A. Supplementary data

Supplementary data to this article can be found online at https://doi.org/10.1016/j.bioactmat.2023.07.026.

References

[1] R. Kuai, L.J. Ochyl, K.S. Bahjat, A. Schwendeman, J.J. Moon, Designer vaccine nanodiscs for personalized cancer immunotherapy, Nat. Mater. 16 (2017) 489–496.
[2] J.L. Liang, G.F. Luo, W.H. Chen, X.Z. Zhang, Recent advances in engineered materials for immunotherapy-involved combination cancer therapy, Adv. Mater. 33 (2021), 202007630.
[3] L. Gravitz, Cancer immunotherapy, Nature 504 (2013). S1–S1.
[4] H. Ledford, Immunotherapy's cancer remit widens, Nature 497 (2013), 544–544.
[5] N.L. Yang, F. Gong, L. Cheng, H.L. Lei, W. Li, Z.B. Sun, C.F. Ni, Z.H. Wang, Z. Liu, Biodegradable magnesium alloy with eddy thermal effect for effective and accurate magnetic hyperthermia ablation of tumors, Natl. Sci. Rev. 8 (2021) nwaa122.
[6] E. Bender, Cancer immunotherapy, Nature 552 (2017), 561–561.
[7] N.L. Yang, F. Gong, Y.K. Zhou, Y. Hao, Z.L. Dong, H.L. Lei, L.P. Zhong, X.Y. Yang, X.W. Wang, Y.X. Zhao, Z. Liu, L. Cheng, A general in-situ reduction method to prepare core-shell liquid-metal/metal nanoparticles for photothermally enhanced catalytic cancer therapy, Biomaterials 277 (2021) 121125.
[8] S. Bai, et al., Ultrasmall iron-doped titanium oxide nanodots for enhanced sonodynamic and chemodynamic cancer therapy, ACS Nano 14 (2020) 15119–15130.
[9] E. Reilly, A. McCavigan, S.M. Walker, N. McCabe, E. Parkes, D.P. Harkin, R. D. Kennedy, L.A. Knight, Exploration of the cGAS-STING pathway in prostate cancer, J. Clin. Oncol. 36 (2018), 103–103.
[10] J. Kwon, S.F. Bakhoum, The cytosolic DNA-sensing cGAS-STING pathway in cancer, Cancer Discov. 10 (2020) 26–39.
[11] M. Motwani, S. Pesiridis, K.A. Fitzgerald, DNA sensing by the cGAS-STING pathway in health and disease, Nat. Rev. Genet. 20 (2019) 657–674.
[12] S.Y. Ding, J. Diep, N.G. Feng, L.L. Ren, B. Li, Y.S. Ooi, X. Wang, K.F. Brulois, L. L. Yasukawa, X.N. Li, C.J. Kuo, D.A. Solomon, J.E. Carette, H.B. Greenberg, STAG2 deficiency induces interferon responses via cGAS-STING pathway and restricts virus infection, Nat. Commun. 9 (2018) 1485.
[13] T. Sen, Identifying and targeting the Achilles heel of a recalcitrant cancer, Sci. Transl. Med. 13 (2021) abj6946.
[14] C.G. Wang, R. Zhang, X.M. Wei, M.Z. Lv, Z.F. Jiang, Metalloimmunology: the metal ion-controlled immunity, Adv. Immunol. 145 (2020) 187–241.
[15] M. Sarhan, W.G. Land, W. Tonnus, C.P. Hugo, A. Linkermann, Origin and consequences of necroinflammation, Physiol. Rev. 98 (2018) 727–780.
[16] X.Q. Sun, Y. Zhang, J.Q. Li, K.S. Park, K. Han, X.W. Zhou, Y. Xu, J. Nam, J. Xu, X. Y. Shi, L. Wei, Y.L. Lei, J.J. Moon, Amplifying STING activation by cyclic dinucleotide-manganese particles for local and systemic cancer metalloimmunotherapy, Nat. Nanotechnol. 16 (2021) 1260–1270, https://doi.org/10.1038/s41565-021-00962-9.
[17] R. Zhang, et al., Manganese salts function as potent adjuvants, Cell. Mol. Immunol. 18 (2021) 1222–1234.
[18] L.L. Tian, Y.X. Wang, L.L. Sun, J. Xu, Y. Chao, K. Yang, S. Wang, Z. Liu, Cerenkov luminescence-induced NO release from P-32-Labeled ZnFe(CN)(5)NO nanosheets to enhance radioisotope-immunotherapy, Matter-Us 1 (2019) 1061–1076.
[19] M.J. Cao, et al., Molybdenum derived from nanomaterials incorporates into molybdenum enzymes and affects their activities in vivo, Nat. Nanotechnol. 16 (2021) 708–716.
[20] L. Cheng, J.J. Liu, X. Gu, H. Gong, X.Z. Shi, T. Liu, C. Wang, X.Y. Wang, G. Liu, H. Y. Xing, W.B. Bu, B.Q. Sun, Z. Liu, PEGylated WS_2 nanosheets as a multifunctional theranostic agent for in vivo dual-modal CT/photoacoustic imaging guided photothermal therapy, Adv. Mater. 26 (2014) 1886–1893.
[21] T.Q. Liu, C. Zhu, X. Chen, G.F. Guan, C.Y. Zou, S. Shen, J.Q. Wu, Y.H. Wang, Z. G. Lin, L. Chen, P. Cheng, W. Cheng, A.H. Wu, Ferroptosis, as the most enriched programmed cell death process in glioma, induces immunosuppression and immunotherapy resistance, Neuro. Oncol. 24 (2022) 1113–1125.
[22] L. Zhao, X.X. Zhou, F. Xie, L. Zhang, H.Y. Yan, J. Huang, C. Zhang, F.F. Zhou, J. Chen, L. Zhang, Ferroptosis in cancer and cancer immunotherapy, Cancer Commun. 42 (2022) 88–116.
[23] B.B. Ding, P. Zheng, F. Jiang, Y.J. Zhao, M.F. Wang, M.Y. Chang, P.A. Ma, J. Lin, MnO(x)Nanospikes as nanoadjuvants and immunogenic cell death drugs with enhanced antitumor immunity and antimetastatic effect, Angew. Chem., Int. Ed. 59 (2020) 16381–16384.
[24] H.L. Lei, X.W. Wang, S. Bai, F. Gong, N.L. Yang, Y.H. Gong, L.Q. Hou, M. Cao, Z. Liu, L. Cheng, Biodegradable Fe-doped vanadium disulfide theranostic nanosheets for enhanced sonodynamic/chemodynamic therapy, Acs Appl. Mater. Inter. 12 (2020) 52370–52382.
[25] C.Y. Wu, Z.L. Liu, Z.X. Chen, D.L. Xu, L.S. Chen, H. Lin, J.L. Shi, A nonferrous ferroptosis-like strategy for antioxidant inhibition-synergized nanocatalytic tumor therapeutics, Sci. Adv. 7 (2021) abj8833.
[26] M.A. Badgley, M.A. Badgley, D.M. Kremer, H.C. Maurer, K.E. DelGiorno, H.J. Lee, V. Purohit, I.R. Sagalovskiy, A. Ma, J. Kapilian, C.E.M. Firl, A.R. Decker, S. A. Sastra, C.F. Palermo, L.R. Andrade, P. Sajjakulnukit, L. Zhang, Z.P. Tolstyka, T. Hirschhorn, C. Lamb, T. Liu, W. Gu, E.S. Seeley, E. Stone, G. Georgiou, U. Manor, A. Iuga, G.M. Wahl, B.R. Stockwell, C.A. Lyssiotis, K.P. Olive, Cysteine depletion induces pancreatic tumor ferroptosis in mice, Science 368 (2020) 85–89.
[27] S. Sen, M. Won, M.S. Levine, Y. Noh, A.C. Sedgwick, J.S. Kim, J.L. Sessler, J. F. Arambula, Metal-based anticancer agents as immunogenic cell death inducers: the past, present, and future, Chem. Soc. Rev. 51 (2022) 1212–1233.
[28] W.M. Wang, M. Green, J.E. Choi, M. Gijon, P.D. Kennedy, J.K. Johnson, P. Liao, X. T. Lang, I. Kryczek, A. Sell, H.J. Xia, J.J. Zhou, G.P. Li, J. Li, W. Li, S. Wei, L. Vatan, H.J. Zhang, W. Szeliga, W. Gu, R. Liu, T.S. Lawrence, C. Lamb, Y. Tanno, M. Cieslik, E. Stone, G. Georgiou, T.A. Chan, A. Chinnaiyan, W.P. Zou, CD8(+) T cells regulate tumour ferroptosis during cancer immunotherapy, Nature 569 (2019) 270–274.
[29] B. Ding, P. Zheng, F. Jiang, Y. Zhao, M. Wang, M. Chang, P. Ma, J. Lin, MnOx nanospikes as nanoadjuvants and immunogenic cell death drugs with enhanced antitumor immunity and antimetastatic effect, Angew Chem. Int. Ed. Engl. 59 (2020) 16381–16384.
[30] L. Zitvogel, G. Kroemer, Interferon-gamma induces cancer cell ferroptosis, Cell Res. 29 (2019) 692–693.
[31] A. Bansal, M.C. Simon, Glutathione metabolism in cancer progression and treatment resistance, J. Cell Biol. 217 (2018) 2291–2298.
[32] L.H. Fu, Y.L. Wan, C. Qi, J. He, C.Y. Li, C. Yang, H. Xu, J. Lin, P. Huang, Nanocatalytic theranostics with glutathione depletion and enhanced reactive oxygen species generation for efficient cancer therapy, Adv. Mater. 33 (2021) 202006892.
[33] H. Lei, X. Wang, S. Bai, F. Gong, N. Yang, Y. Gong, L. Hou, M. Cao, Z. Liu, L. Cheng, Biodegradable Fe-doped vanadium disulfide theranostic nanosheets for enhanced sonodynamic/chemodynamic therapy, ACS Appl. Mater. Interfaces 12 (2020) 52370–52382.
[34] M. Gao, J. Yi, J. Zhu, A.M. Minikes, P. Monian, C.B. Thompson, X. Jiang, Role of mitochondria in ferroptosis, Mol Cell 73 (2019) 354–363.
[35] F.J. Bock, S.W.G. Tait, Mitochondria as multifaceted regulators of cell death, Nat. Rev. Mol. Cell Biol. 21 (2020) 85–100.
[36] H. Zhang, et al., CAF secreted miR-522 suppresses ferroptosis and promotes acquired chemo-resistance in gastric cancer, Mol. Cancer 19 (2020) 43.
[37] N. Yang, F. Gong, B. Liu, Y. Hao, Y. Chao, H. Lei, X. Yang, Y. Gong, X. Wang, Z. Liu, L. Cheng, Magnesium galvanic cells produce hydrogen and modulate the tumor microenvironment to inhibit cancer growth, Nat. Commun. 13 (2022) 2336.
[38] D.C. Fajgenbaum, C.H. June, Cytokine storm, N. Engl. J. Med. 383 (2020) 2255–2273.
[39] C. Turnquist, B.M. Ryan, I. Horikawa, B.T. Harris, C.C. Harris, Cytokine storms in cancer and COVID-19, Cancer Cell 38 (2020) 598–601.